RSC Advances

PAPER

View Article Online
View Journal | View Issue



Cite this: *RSC Adv.*, 2025, **15**, 29439

# Catalytic engineering of a cerium vanadate–bismuth vanadate system to yield a bifunctional photocatalyst for simultaneous hydrogen generation and pollutant degradation

Jil Rose Perutil,[ab] Mathew K. Francis,[a] Manish Verma[a] and Neena S. John *[a]

A cerium vanadate–bismuth vanadate (CV–BV) composite is developed to facilitate dual functionality in photocatalytic hydrogen generation and degradation and is synthesized *via* a one pot hydrothermal method. Despite its strong pollutant degradation capability, BV remains ineffective for hydrogen evolution, whereas CV, with favourable band position, actively participates in hydrogen evolution. BV shows a pollutant degradation rate of 90% in 1 hour but does not produce hydrogen, while CV exhibits a hydrogen evolution rate of 590.0 μmol $h^{-1}$ $g^{-1}$ but only a 10% degradation of methyl orange (MO) for the same duration. Notably, the CV–BV heterojunction, governed by an S-scheme mechanism that favours charge carrier separation and redox potential, exhibits excellent performance, simultaneously achieving a hydrogen evolution rate of 1011 μmol $h^{-1}$ $g^{-1}$ and a 98% degradation efficiency for MO. The total organic carbon analysis indicates 93% removal of organic carbon from the dye solution. The system maintains stable catalytic performance over five consecutive cycles, indicating its durability. The solar-to-hydrogen (STH) efficiency for the CV–BV system is determined to be 3.99%. The activity of the CV–BV catalyst is demonstrated in actual wastewater, achieving 96% dye degradation and 803.0 μmol $h^{-1}$ $g^{-1}$ hydrogen generation. Its dual performance remained effective even in MO-contaminated seawater (310.0 μmol $h^{-1}$ $g^{-1}$ and 98% MO degradation), proving its adaptability to harsh, complex environments. The heterojunction efficiently absorbs a broad light spectrum, generating electron–hole pairs, and conduction band electrons of CV participate in proton reduction to produce hydrogen in the presence of a hole scavenger while superoxide radicals partake in degradation as proven from the radical trapping experiments. The synergistic S-scheme charge transfer mechanism within the CV–BV system enhances its bifunctional efficiency, demonstrating significant potential for fuel generation from wastewater with simultaneous environmental remediation.

Received 10th June 2025
Accepted 5th August 2025

DOI: 10.1039/d5ra04077a

rsc.li/rsc-advances



## Introduction

Sustainability and progress in the modern world rely on addressing critical energy and environmental challenges through innovative scientific research. The depletion of non-renewable energy sources has paved the way for the exploration of hydrogen energy, while water pollution has driven advancements in pollutant degradation strategies. Photocatalysis has found significant applications in the field of hydrogen evolution,[1] pollutant degradation,[2,3] $CO_2$ fixation[4] and organic synthesis.[5] The construction of a photocatalyst with bifunctional properties can offer a practical and cost-effective solution to address fuel generation and environmental remediation. To ensure efficient performance, a photocatalyst must meet several critical criteria: (1) improved light absorption properties to maximize the use of the available light spectrum, (2) enhanced separation and transfer of photogenerated electron–hole pairs to reduce recombination losses, and (3) optimized valence and conduction band positions for optimal alignment with the redox potential of the reactant species. These factors play a crucial role in determining the catalytic performance of the material.[6] Simultaneous hydrogen evolution and pollutant degradation further enhance the practicality of such photocatalysts, offering a sustainable approach to address both energy and environmental concerns. By efficiently utilizing solar energy, this dual-function system not only generates hydrogen fuel but also degrades harmful pollutants, ensuring effective waste management while contributing to renewable energy production. In a recent review by Kumar *et al.*, advancements in coupled photocatalytic systems for simultaneous hydrogen generation and pollutant removal are analysed.[7] A few photocatalysts including metal-doped and

[a]*Centre for Nano and Soft Matter Sciences (CeNS), Shivanapura, Bengaluru 562162, India. E-mail: jsneena@cens.res.in*
[b]*Manipal Academy of Higher Education, Manipal 576104, India*

heterojunction systems exhibiting degradation performance in the range of 5.3–100% and hydrogen evolution rates of 13.7–2724.89 μmol $g^{-1}$ $h^{-1}$ are presented in the above review. Yu *et al.* have reported a type-II heterojunction photocatalyst, Ni-MOF derivative-CdS-DETA/g-$C_3N_5$, for simultaneous dye degradation and hydrogen evolution, achieving a high $H_2$ evolution rate of 2974.4 μmol $g^{-1}$ $h^{-1}$ and 99.97% rhodamine B (RhB) removal.[8]

In the present work, we have exploited the heterojunction in bismuth–cerium vanadate composite combining their advantages to achieve an efficient bifunctional photocatalyst. Bismuth vanadate, a widely used photocatalyst, offers numerous advantages as a photocatalytic material as it is nontoxic, highly stable, exhibiting photocatalytic performance under visible-light irradiation due to suitable band gap and valence band edge for driving oxidation.[9–11] Despite its many advantages, the conduction band (CB) potential of bismuth vanadate is relatively positive, not suitable for hydrogen generation. The strategy adopted to enable $H_2$ production involves coupling bismuth vanadate with a semiconductor that has a more negative CB potential, creating a heterojunction for improved photocatalytic performance.[12–14] For example, Li *et al.* has introduced $BiVO_4/ZnIn_2S_4$ (BZS) Z-scheme photocatalyst achieving remarkable hydrogen evolution of 2.243 mmol $g^{-1}$ $h^{-1}$ under visible light in a triethanolamine solution.[12] $BiVO_4/TiO_2$ nanocomposite with 0.5 wt% Pt has shown $H_2$ production rate over 100 times higher than bare $BiVO_4/TiO_2$, following a Z-scheme mechanism for efficient charge transfer.[15] $BiVO_4$-OVs/g-$C_3N_4$ photocatalysts have been designed with oxygen vacancies (OVs) at the hetero-interface, where defect states in the $BiVO_4$ bandgap acted as intermediaries for carrier recombination showing bifunctional properties with enhanced pollutant degradation rates for rhodamine B and tetracyclines as well as hydrogen production rate of 558 μmol $g^{-1}$ $h^{-1}$ using triethanolamine as a hole scavenger and Pt as a cocatalyst.[16]

Here, we have employed cerium vanadate, a rare earth vanadate, to couple with Bi-vanadate to form a heterojunction imparting the capability of both organic degradation and hydrogen evolution from textile wastewater. Ce-vanadate possesses a zircon-type tetragonal structure characterized by the edge-sharing arrangement of ($CeO_9$) polyhedra and alternating [$VO_4$] tetrahedra.[17] The exceptional redox and optical properties of cerium vanadate as a ternary metal oxide catalyst are attributed to the multiple electronic transitions of its lanthanide component. The partially filled 4f orbitals of cerium and oxygen vacancies contribute to narrowing of bandgap to 2–2.5 eV. The broad light absorption capability enhances its photocatalytic performance under both UV and visible light. Cerium vanadate is widely used in applications such as sensors,[18] batteries,[19] photocatalysis,[20] and biomedical treatment,[21] owing to its favourable physical and chemical properties and low toxicity. Both theoretical and experimental studies highlight the crucial role of the coexistence of $Ce^{4+}$ and $Ce^{3+}$ ions at the surface of cerium vanadate nanostructures, which serve as the primary catalytic sites and significantly contribute to its enhanced photocatalytic activity. Additionally, cerium vanadate and bismuth vanadate have similar crystal structure, which facilitate the formation of a better heterojunction interface that might enhance photocatalytic performance by reducing charge recombination.[22] The reported studies include a novel Z-scheme $CeO_2/CeVO_4/V_2O_5$ photocatalyst, synthesized through solid-phase reaction that has shown 93% degradation of methylene blue with generation of hydrogen at a rate of 200 μmol $h^{-1}$ $g^{-1}$ under visible-light irradiation.[23] The S-scheme heterojunction formed at $Zn_{0.5}Cd_{0.5}S/CeVO_4$ interface has shown a hydrogen yield of 695.55 μmol in 5 hours in 10% lactic acid.[24] Noh *et al.* have used Pt–$CeVO_4$ nanocomposites with precisely controlled amounts of Pt nanoparticles on $CeVO_4$ as a photocatalyst, achieving a remarkable hydrogen production rate of 220.68 mmol $g^{-1}$ $h^{-1}$ using triethanolamine as the sacrificial donor.[25] The Z-scheme $ZnO/CeVO_4$ heterostructure with enhanced electron interaction, light absorption, and carrier separation has exhibited hydrogen production rate of 1289 μmol $g^{-1}$ $h^{-1}$ in presence of $Na_2S/Na_2SO_3$ as a sacrificial agent.[26]

We have designed a cerium vanadate–bismuth vanadate (CV–BV) composite combining the advantages of both the components and examined its capability towards fuel generation from pollutant laden water. Interestingly, the coupling of BV with CV enhances its photocatalytic performance, specifically for simultaneous hydrogen evolution and pollutant degradation in aqueous medium. Detailed characterization and photocurrent measurement are conducted and the CV–BV heterojunction, significantly improves charge carrier separation and redox potential, demonstrating exceptional photocatalytic performance with a hydrogen evolution rate of 1011 μmol $h^{-1}$ $g^{-1}$ and 98% degradation efficiency for methyl orange (MO). The system maintains stable catalytic performance for over five consecutive cycles. Mechanistic studies indicate that the CV–BV system generates a higher number of photogenerated charge carriers, exhibits reduced recombination rates, and demonstrates lower charge transfer resistance compared to the individual components. Furthermore, radical trapping experiments reveal the critical role of superoxide radicals in the degradation of MO. An S-scheme based heterojunction is proposed to explain the superior photocatalytic properties of CV–BV heterojunction. The high performance, stability, and effectiveness in actual systems such as seawater and spent textile wastewater is also demonstrated. The CV–BV photocatalyst has achieved hydrogen evolution rate of 310.0 μmol $h^{-1}$ $g^{-1}$ in seawater and 803.0 μmol $h^{-1}$ $g^{-1}$ along with 96% pollutant degradation in textile wastewater. These results highlight its potential as a multifunctional material to address pressing global challenges of energy scarcity and environmental pollution.

## Experimental section

### Materials

The chemicals were obtained from commercial sources and were used without any further purification. Cerium nitrate hexahydrate ($Ce(NO_3)_3 \cdot 6H_2O$, ≥98.5%), bismuth acetate ($(CH_3COO)_3Bi$, ≥99.99%), hydrazine hydrate ($N_2H_4$ 50–60%) and methyl orange ($C_{14}H_{14}N_3NaO_3S$) were purchased from Sigma-Aldrich. Ammonium metavanadate ($NH_4VO_3$, ≥99.00%) was purchased from Finar.

### Synthesis of CV–BV composite

A cerium vanadate–bismuth vanadate (CV–BV) composite was synthesized using a facile hydrothermal process.[27] Adequate amount of (1) cerium nitrate hexahydrate ($Ce(NO_3)_3 \cdot 6H_2O$) and Bismuth acetate $Bi(CH_3COO)_3$, (2) ammonium metavanadate ($NH_4VO_3$) were dissolved in 5 mL of distilled water, creating the first and second solutions, respectively. The second solution was added to the first, and the mixture was stirred at 40 °C for 10 minutes. Subsequently, hydrazine and distilled water were added to this mixture, which was then stirred for another 10 minutes. The resulting solution was transferred to an autoclave and heated at 180 °C for 10 hours. After allowing the autoclave to cool to ambient temperature, the precipitate was collected, washed several times with ethanol and distilled water, and then dried at 60 °C for 8 hours.

### Characterization methods

X-ray diffraction (XRD) patterns were obtained using a Smartlab diffractometer (Rigaku) with CuKα incident radiation (40 kV and 30 mA) in parallel beam mode. The morphology of the substrate was examined utilizing a field emission scanning electron microscope (FESEM) from TESCAN – MIRA 3 equipped with energy-dispersive spectrometry (Bruker Quantax 200). FESEM images were collected after drop-casting an ethanolic suspension of CV–BV onto a Si substrate. UV-vis diffuse reflectance spectra were acquired using a Lambda 750 UV-VIS-NIR spectrophotometer (PerkinElmer) in diffuse reflectance mode. High-resolution transmission electron microscopy (HRTEM) at 200 kV with a TALOS F200S G2 instrument (Thermo Fisher) was employed for detailed structural and morphological characterization, electron diffraction, and elemental mapping. The sample was dispersed in ethanol drop-cast and dried on the TEM grid for imaging. X-ray photoelectron spectra (XPS) of the samples were acquired using a K-Alpha X-ray photoelectron spectrometer (Thermo Fisher). It features a 180° double focusing hemispherical analyzer with a 128-channel detector and an Al K-Alpha micro-focused monochromator X-ray source with a variable spot size. The photoluminescence spectra of the samples were acquired from solid powders by Horiba Jobin Yvon Fluorolog-3, equipped with a 300 W xenon lamp as the excitation source. Photocurrent studies and electrochemical impedance spectroscopy (EIS) measurements were recorded on an electrochemical workstation (CHI-760E). The degradation products of MO were analysed using liquid chromatography-mass spectrometry (LC-MS) on a Shimadzu LCMS 2020 system equipped with a single quadrupole mass spectrometer. The total organic carbon (TOC) analysis of the MO dye solution before and after the photocatalysis was conducted using a Total Organic Carbon Analyzer (Analytik Jena – Multi N/C 2100) using the APHA 5310B method.

### Photocatalytic hydrogen evolution and degradation studies

The photocatalytic performances of the prepared photocatalyst were evaluated by using the aqueous solution of 20 ppm (20 mg $L^{-1}$) methyl orange dye (MO). The photocatalytic experiments were performed to explore the simultaneous hydrogen evolution and pollutant degradation of CV–BV composite. Before starting the bifunctional photocatalytic experiment, the reaction system was purged with nitrogen. A 270 W xenon lamp served as the light source. A 75 mL solution containing methyl orange (20 mg $L^{-1}$), 10 mg of photocatalyst, and $Na_2S/Na_2SO_3$ as a sacrificial agent was placed in a quartz cell. For degradation studies, about 3 mL of an aliquot from a reaction mixture was removed every 15 minute intervals during light exposure, and the absorbance of the supernatant was measured using a UV-vis spectrophotometer, as there is a linear relationship between absorbance ($A$) and MO concentration ($C$) to understand the progression of degradation. The degradation rate ($\eta$) of MO was calculated using the formula,

$$\eta = \frac{C_0 - C_t}{C_0} \times 100\% = \frac{A_0 - A_t}{A_0} \times 100\%, \quad (1)$$

where $A_0$ or $C_0$ and $A_t$ or $C_t$ represent the initial and the absorbance or concentration at reaction time '$t$', respectively. In the case of photocatalytic hydrogen evolution experiment, the headspace of the cell was periodically sampled by withdrawing aliquots at 2 hour intervals using a 5 mL airtight syringe. These collected samples were then injected into a gas chromatography with a thermal conductivity detector (Agilent 490 micro-GC) and the amount of $H_2$ was evaluated from the calibration graphs.

Solar to hydrogen conversion efficiency (STH) was computed using the following formula,

$$\text{STH}\ (\%) = \frac{\text{the output energy as hydrogen}}{\text{energy of the incident light}} \times 100 \quad (2)$$

$$\text{STH}\ (\%) = \frac{r_{H_2}\ (\text{mmol s}^{-1}) \times \Delta G\ (237\,000\ \text{J mol}^{-1})}{P_{\text{light}}\ (\text{mW cm}^{-2}) \times A\ (\text{cm}^2)} \times 100, \quad (3)$$

where $\Delta G$ is the gain in Gibbs free energy (J $mol^{-1}$), and $r_{H_2}$ is the rate of hydrogen generation (mmol $s^{-1}$). The irradiated sample area, $A$, is measured in $cm^2$, and the energy flux of incident light $P_{light}$, is measured in mW $cm^{-2}$.

The photocurrent measurement was performed at an applied potential of 0.8 V *vs.* Ag/AgCl using a standard three-electrode system consisting of catalyst coated FTO (fluorine doped tin oxide, 2 × 1 $cm^2$) as the working electrode, Pt foil as the counter electrode, and the standard calomel electrode as the reference electrode in 0.5 M aqueous sodium sulphate as the electrolyte. The catalyst ink was prepared by mixing 2 mg of catalyst and 50 μL of Nafion (2% w/w in water and 1-propanol) in 200 μL of ethanol and sonicated for 60 min. Subsequently, the sample (100 μL) was drop-cast over the FTO and dried at room temperature for use as the working electrode. Xe lamp (270 W) was used as the source of irradiation. Electrochemical impedance spectroscopy (EIS) was performed employing the similar three electrode system (0.8 V *vs.* Ag/AgCl) in a frequency range of $10^5$ to $10^{-2}$ Hz with the amplitude of the sinusoidal wave set to ±5 mV.

To understand the extent of dye degradation and mineralization, we have performed total organic carbon (TOC) analysis. The TOC analysis was done using a Total Organic Carbon

Analyzer before and after the photocatalysis of the MO dye using the APHA 5310B method. The TOC removal efficiency was calculated as

$$\text{TOC removal } (\%) = \frac{\text{TOC}_\text{i} - \text{TOC}_t}{\text{TOC}_\text{i}} \times 100, \quad (4)$$

where $\text{TOC}_\text{i}$ and $\text{TOC}_t$ are the total organic carbon concentrations (mg $L^{-1}$) of the MO dye before and after photocatalysis, respectively.

## Results and discussion

### Characterization of CV–BV system

The X-ray diffraction data of CV–BV, synthesised by a single pot hydrothermal method, is shown in Fig. 1. The peaks of CV–BV can be assigned to the individual peaks of cerium vanadate (CV) and bismuth vanadate (BV). The CV in the composite exhibits two phases; a monoclinic structure of $CeVO_4$ with a $P2_1/n$ space group with major peaks at 37.90°, 39.60° and 48.70° corresponding to the planes (022), (130) and (023), respectively and tetragonal structure of $CeVO_4$ showing peaks at 24.20°, 32.50°, 34.30° and 48.00° corresponding to the lattice planes of (200), (112), (220) and (312), respectively. The BV component shows a monoclinic structure with a $I2/m$ space group showing major peaks at 27.90°, 46.03° and 56.10° that corresponds to the planes (101), (020) and (103) of $Bi_7VO_{13}$. As shown in Fig. 2(a), pristine CV exhibits excellent absorption in both the ultraviolet and visible regions, while pristine BV demonstrates good absorption in the 200–500 nm range.[22] Due to the incorporation of CV, the optical absorbance of the resulting CV–BV samples is seen enhanced compared to BV and CV. This implies enhanced light absorption by CV–BV and electron–hole generation. The band gaps of BV and CV are estimated to be 2.20 and 2.46 eV, respectively, using Tauc plot analysis and are shown in Fig. S1.

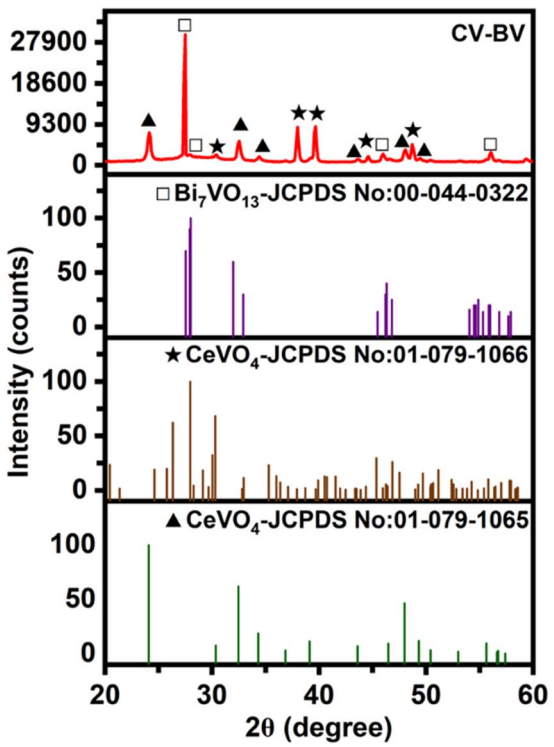


Fig. 1 X-ray diffraction data of CV–BV composite along with simulated standard patterns (JCPDS) of CV and BV.

The photoluminescence (PL) spectra of BV, CV and CV–BV under excitation at 360 nm are shown in Fig. 2(b). It can be distinctly observed that pristine CV shows a strong emission peak at 384 nm and also at 398 nm, likewise, BV shows peaks at 384 and 398 nm. Notably, the PL intensity of CV–BV is significantly reduced compared to that of individual components. This quenching of luminescence indicates that the recombination of charge carriers is effectively suppressed due to the interaction of CV and BV, which facilitates the formation of a junction thereby enhancing the efficient separation of photogenerated charge carriers under illumination.

The FESEM images of CV–BV exhibit nanosized crystallites as shown in Fig. 3(a). The morphology and structure of the CV–BV samples are characterized in detail using HRTEM. As illustrated in Fig. 3(b) and (c), CV–BV displays a nanocrystalline structure comprising phases of CV and BV. HRTEM images given in Fig. 3(c) and (d) reveals intimate junctions formed between CV and BV. The measured lattice spacings in Fig. 3(d), 0.19 nm and 0.32 nm, corresponds to the (020) and (101) planes of monoclinic BV, respectively. Likewise, the spacings of 0.37 nm and 0.27 nm are associated with the (200) and (112) planes of tetragonal CV while the spacing of 0.24 nm corresponds to the (022) plane of monoclinic CV. The energy-dispersive X-ray spectroscopy (EDS) elemental mapping, presented in Fig. S2, verifies the distribution of Ce, Bi, V, and O elements throughout the CV–BV composite. This observation is further supported by the EDS spectra and composition analysis provided in Fig. S3(a) and Table S1, which distinctly confirms the presence of all constituent elements of CV–BV. Additionally, the particle size distribution derived from the TEM image, Fig. S3(b), indicates the particle size range as 20 nm to 70 nm and an average particle size of 41 nm.

The chemical composition and electronic states of the prepared CV–BV samples are analysed using XPS. The survey XPS spectra (Fig. S4) reveal that the sample primarily comprises Bi, Ce, V, O, and C elements. The Ce 3d spectra (Fig. 4(a)) exhibit a complex convolution with multiplet of Ce $3d_{3/2}$ and Ce $3d_{5/2}$, which are deconvoluted into eight peaks using Gaussian fitting. Peaks at approximately 883.58 eV (v) and 889.20 eV (v″) in the lower binding energy region, along with 903.00 eV (u) and 907.60 eV (u″) in the higher binding energy region, are assigned to $Ce^{4+}$, corresponding to Ce $3d_{5/2}$ and Ce $3d_{3/2}$, respectively.[28,29] Similarly, peaks at 881.00 eV ($v_0$), 886.00 eV (v′), 900.02 eV ($u_0$), and 904.50 eV (u′) are attributed to $Ce^{3+}$, associated with Ce $3d_{5/2}$ and Ce $3d_{3/2}$, respectively. These results confirm the presence of both $Ce^{3+}$ and $Ce^{4+}$ valence states in the sample. In the high-resolution Bi 4f XPS spectra, two prominent peaks at 159.22 eV and 164.30 eV correspond to the spin–orbit splitting of Bi $4f_{7/2}$ and Bi $4f_{5/2}$, respectively, confirming the presence of $Bi^{3+}$ cations in the CV–BV photocatalyst (Fig. 4(b)).[22] Peaks at 516.90 eV and 524.10 eV correspond to V $2p_{3/2}$ and V $2p_{1/2}$, respectively, confirming the presence of $V^{5+}$ in the CV–BV

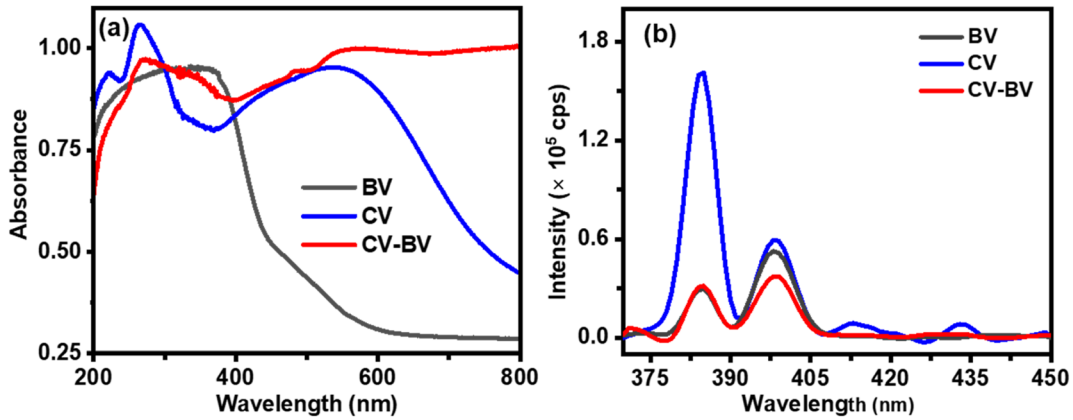


Fig. 2 (a) UV-vis absorption spectra (b) PL spectra of BV, CV and CV–BV systems.

composite as shown in Fig. 4(c). Additionally, a peak at 521.00 eV is attributed to the O 1s satellite.[30] Further analysis of the O 1s spectra (Fig. 4(d)) reveals an asymmetric peak that is deconvoluted into three components at 529.90 eV, 531.30 eV, and 534.30 eV, attributed to lattice oxygen ($O_1$), defective site oxygen ($O_2$), and hydroxyl/surface-adsorbed oxygen species ($O_3$), respectively.[30,31] The presence of oxygen vacancies ($O_2$) plays a critical role in trapping photoinduced electrons, enhancing charge carrier separation, and reducing the recombination of photoinduced electron–hole pairs.

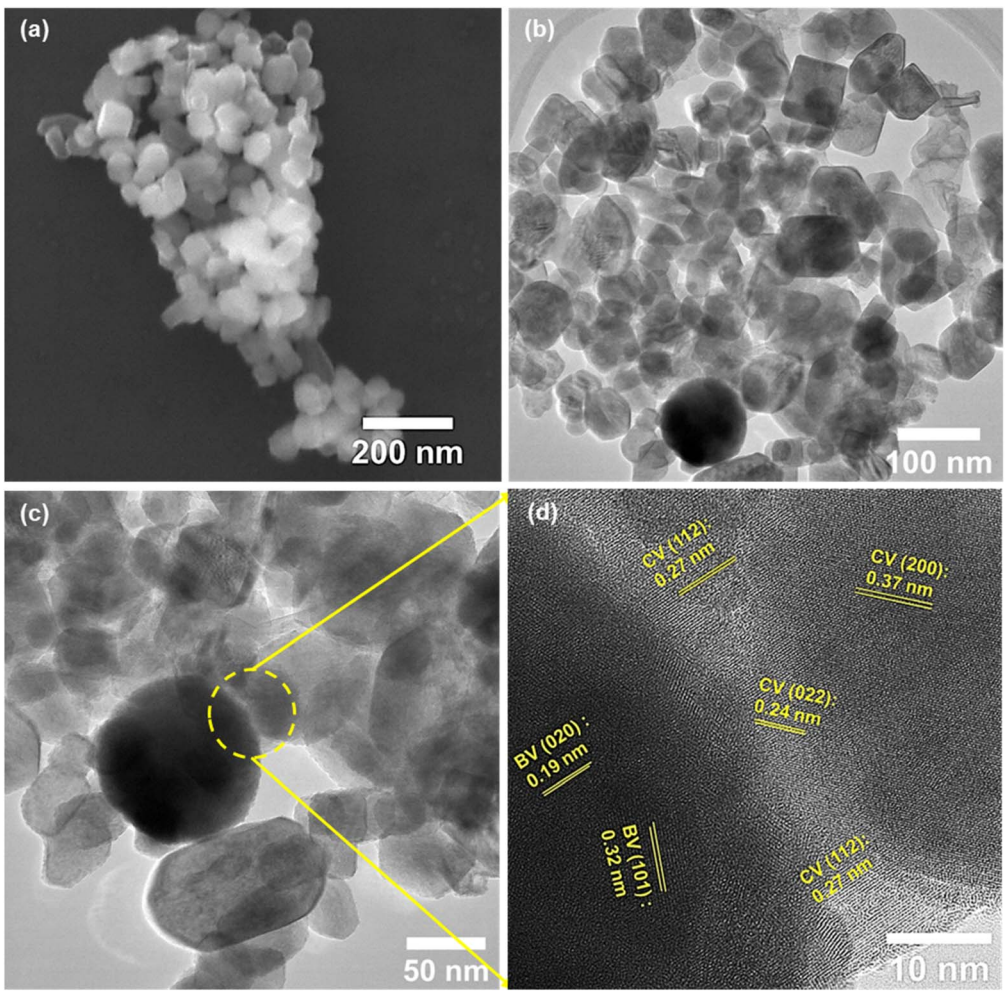


Fig. 3 (a) FESEM image of CV–BV composite (b and c) TEM images (d) HR-TEM image showing lattice planes resolved for CV–BV interface.

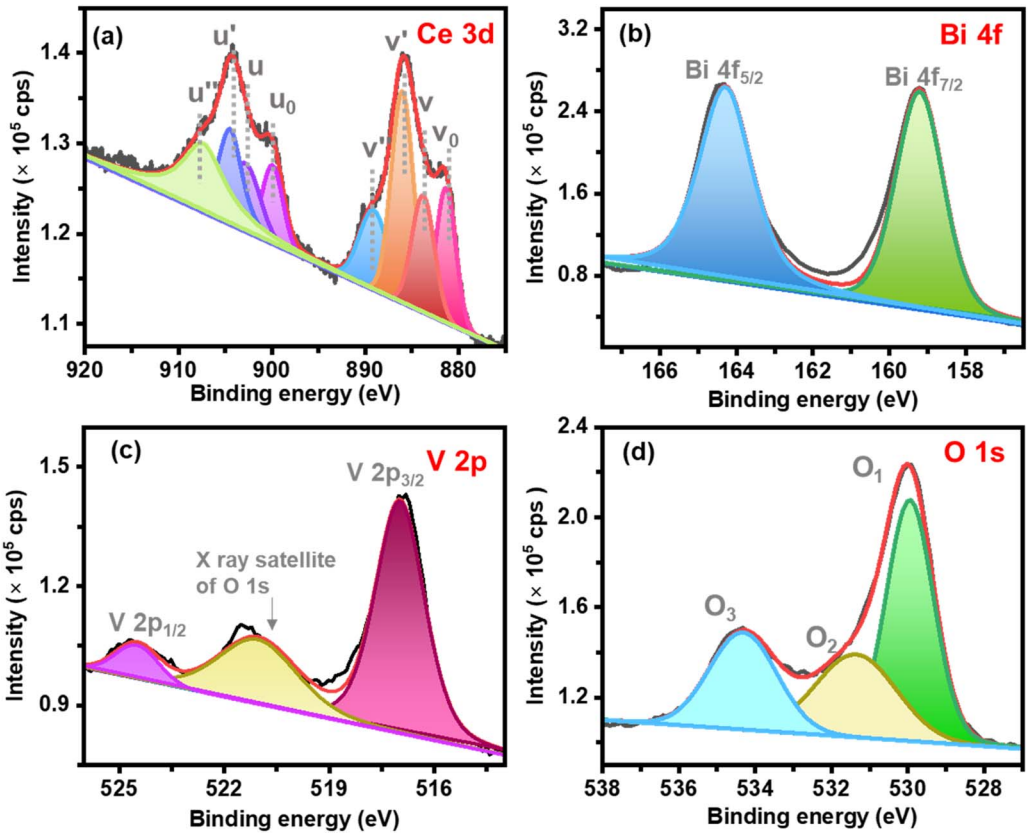


Fig. 4 XPS spectra of CV–BV photocatalyst (a) Ce 3d (b) Bi 4f (c) V 2p and (d) O 1s.

As shown in Fig. 5(a), the arc radius of Nyquist plots of the CV–BV junction is smaller than those of pristine BV and CV, implying the decreased charge transfer resistance, quick interfacial charge transfer process, and an effective separation of photoinduced charge carriers. The generation and transfer of photoinduced charge carriers during the photocatalytic process can be studied using transient photocurrent responses. In general, a higher photocurrent density typically indicates a greater number of photoinduced electron–hole pairs, leading to enhanced photocatalytic activity. The transient photocurrent responses of pristine BV, CV and CV–BV are recorded for several on–off cycles under light irradiation. As can be seen in Fig. 5(b), the CV–BV exhibit an obvious increase in the photocurrent densities, compared to pristine BV and CV samples.

### Photocatalytic $H_2$ evolution and pollutant degradation

The simultaneous photocatalytic experiments for $H_2$ production and MO degradation are conducted in the same reaction system, which contained 20 ppm MO, $Na_2S/Na_2SO_3$, and 10 mg

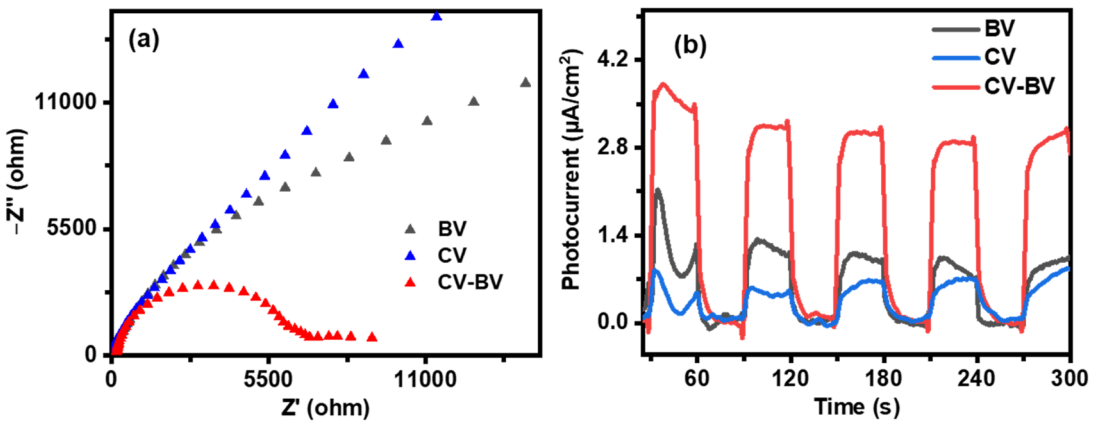


Fig. 5 (a) Nyquist plot (b) Photocurrent response of BV, CV, and CV–BV composite.

of CV–BV as bifunctional photocatalysts in water under Xe lamp irradiation of 270 W with 100 mW $cm^{-2}$ output intensity. The degradation is monitored by UV-vis spectroscopy while $H_2$ evolution is measured by gas chromatography at regular intervals. The standard calibration curve used for hydrogen quantification is given in Fig. S5 and the GC traces for $H_2$ evolution for all samples are provided in Fig. S17. Fig. 6(a) presents the UV-vis absorbance data of MO dye recorded at 15 minute intervals, with a maximum absorbance observed at 462 nm that diminishes over 1 hour. The spectra clearly reveal significant degradation of the dye within just one hour of reaction, indicating the efficient utilization of charge carriers within the CV–BV composite. The peak absorbance ($A$) at any time is proportional to the concentration of the analyte at that time, and hence, $A_t/A_0$ is proportional to $C_t/C_0$ where $C_t$ is the concentration at time '$t$' and $C_0$ represents the initial concentration after equilibration in dark. The plot of $A_t/A_0 \sim C_t/C_0$ *versus* time is given in Fig. 6(b). The CV–BV composite exhibits a markedly improved photocatalytic degradation efficiency compared to CV alone, confirming a synergistic enhancement effect. The corresponding UV-vis absorption spectra of photocatalytic degradation of MO dye using pristine CV and BV are shown in Fig. S6. Fig. 6(c) represents the hydrogen evolution rate of the CV–BV heterojunction over a duration of four hours, demonstrating its superior photocatalytic activity. As shown in the Fig. 6(d), BV has shown a good pollutant degradation rate of 90% after 1 hour but is not capable of hydrogen evolution while CV shows a hydrogen evolution rate of 590.0 μmol $h^{-1}$ $g^{-1}$ and MO degradation rate of 10% in 1 hour.

However, the bifunctional system, CV–BV has achieved an enhanced hydrogen evolution rate of 1011 μmol $h^{-1}$ $g^{-1}$ and MO degradation rate of 98%. The suitable band levels for hydrogen production, along with the reduced charge recombination rate in the CV–BV system, enhance hydrogen evolution and degradation activities compared to the pristine CV and BV as confirmed by the aforementioned data. Table S3 provides a comparison of the degradation efficiency and hydrogen yield for bifunctional systems reported for simultaneous photocatalytic hydrogen production and pollutant degradation.

Solar to hydrogen (STH) efficiency is a critical parameter in evaluating the performance of a photocatalyst for solar-driven hydrogen production.[32] The STH efficiency for CV–BV system, calculated using eqn (3), is determined to be 3.99%. A higher STH efficiency reflects the ability of a photocatalyst to effectively convert solar energy into hydrogen energy, highlighting its potential for sustainable energy applications.

LC-MS analysis (Fig. S7(a)) is used to identify the degradation products and intermediates, revealing that MO degradation proceeds through multiple intermediates. An asymmetric cleavage of MO results in an $m/z$ value of 227, and the

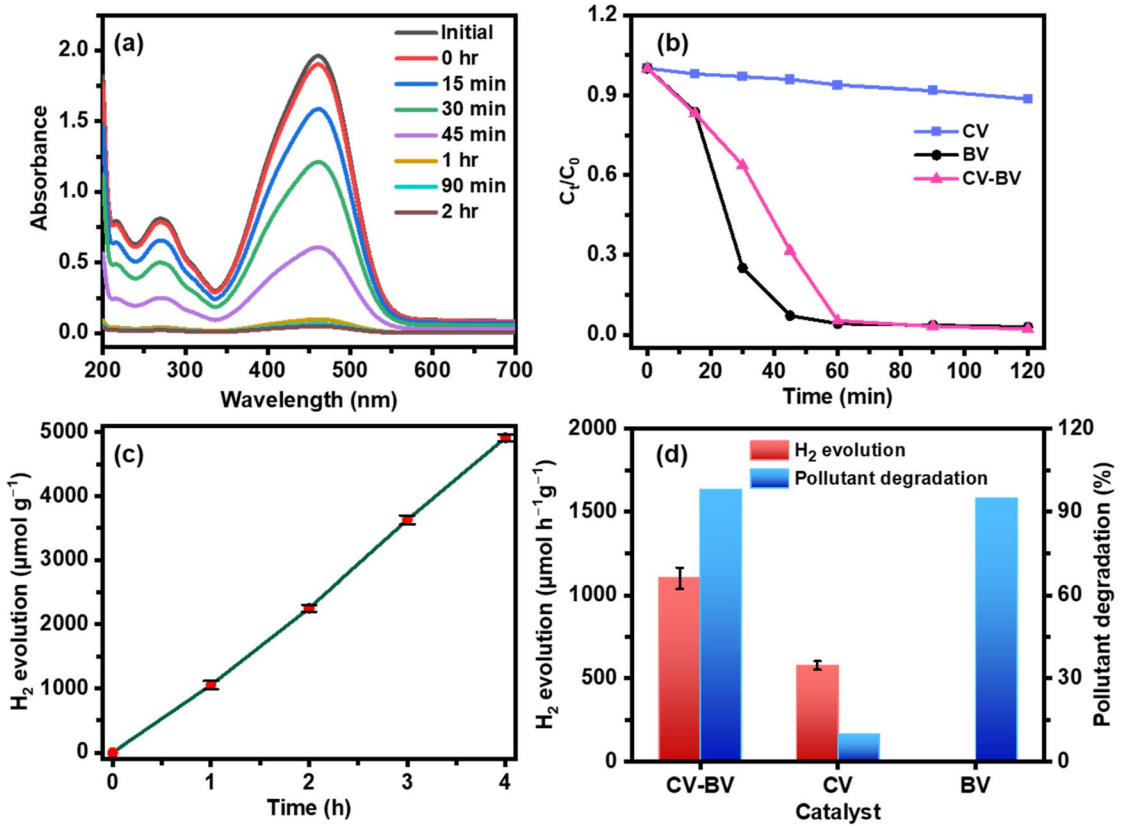


Fig. 6 (a) UV-vis spectra showing photocatalytic degradation of 20 ppm MO dye in the presence of CV–BV catalyst (b) time dependent degradation kinetics of MO in presence of individual components and composite (c) $H_2$ evolution rate of CV–BV catalyst (d) bar diagram of the comparative activity of CV–BV, CV and BV photocatalysts during simultaneous MO degradation and $H_2$ evolution.

breakdown of the N=N bond forms *N*,*N*-dimethyl-*p*-phenylenediamine ($m/z = 137$)[33,34] that further degrades into smaller components ($m/z = 105$).[35] The TOC analysis is done before and after the photocatalysis of the MO dye in presence of CV–BV catalyst for 2 h (eqn (4)). The TOC is seen to decrease drastically from 313 to 20 mg $L^{-1}$, which corresponds to 93% removal of the dye. A schematic illustration of the possible degradation pathway is depicted in Fig. S7(b).

Various control experiments were performed for optimizing the CV–BV ratio and photocatalyst dosage. To investigate the influence of the cerium-to-bismuth precursor molar ratio on the overall performance of the system, two different ratios, CV(1)–BV(2) and CV(1)–BV(0.5), are also examined for hydrogen evolution and pollutant degradation studies, along with that of CV–BV (CV(1)–BV(1)), wherein Ce to Bi precursor molar ratio is 1 : 1. The XRD patterns of the control samples, along with CV–BV and their corresponding standard JCPDS files, are presented in Fig. S8(a)–(f). It is evident that no significant shift or alteration in peak positions is observed among CV–BV and the control samples. Notably, CV(1)–BV(0.5) exhibits more intense diffraction peaks corresponding to CV, particularly at $2\theta$ values of 24.1°, 32.4°, and 47.9°, which can be attributed to its greater proportion of CV relative to BV in the composite. The optical characterization of control samples performed using UV-vis absorption spectra is shown in Fig. S8(g). All samples exhibit strong UV and visible light absorption, highlighting their photocatalytic potential. Notably, CV(1)–BV(0.5) shows higher UV absorption than CV(1)–BV(2) and CV–BV, likely due to its higher CV content. As shown in Fig. 7(a), varying the molar ratio of Bi-precursor has minimal impact on the degradation performance, as confirmed by the degradation kinetic plots. However, the CV(1)–BV(1) composition exhibits optimal degradation performance. The corresponding UV-vis spectra of the samples are presented in Fig. S9(a) and (b). In contrast, hydrogen evolution shows a marked dependence on the ratio of cerium to bismuth precursor (Fig. 7(b)). Notably, the CV(1)–BV(2) system has achieved a methyl orange (MO) degradation efficiency of 98% along with a hydrogen evolution rate of 500.0 μmol $h^{-1}$ $g^{-1}$. On the other hand, the CV(1)–BV(0.5) system shows a slightly lower MO degradation rate of 93%, but with a significantly reduced hydrogen evolution rate of 150.0 μmol $h^{-1}$ $g^{-1}$. These findings highlight the crucial role of molar ratio of the components in optimizing performance, with the optimal composition identified as CV(1)–BV(1) or CV–BV. Optimization studies of catalytic dosage have revealed that 10 mg of CV–BV is the optimal quantity to achieve better hydrogen yield, as shown in Fig. S10. When the dosage is increased to 25 mg, hydrogen evolution decreased, likely due to the reduced light absorption of the system, as the catalyst appearance is black in colour. Conversely, using only 5 mg of the catalyst has resulted in minimal hydrogen evolution.

Furthermore, the degradation efficiency is tested for another pollutant dye from textile industry, rhodamine B, along with $H_2$ evolution and the simultaneous bifunctional activity is also tested in sea water and actual textile wastewater. Fig. 8(a) depicts the UV-vis absorbance spectra for 20 ppm RhB solution in the presence of CV–BV catalyst in DI water. The catalyst demonstrated effective degradation performance, achieving 45% degradation of RhB in 2 h and also achieved a hydrogen evolution rate of 722.0 μmol $h^{-1}$ $g^{-1}$ in the RhB-DI water system (Fig. 8(c)).

Additionally, Fig. 8(b) shows the UV-vis absorbance spectra of MO dye tested in seawater and shows an impressive 98% degradation of MO and 310.0 μmol $h^{-1}$ $g^{-1}$ of hydrogen evolution (Fig. 8(c)). The use of seawater in photocatalysis is crucial as it reflects a more sustainable and environmentally relevant medium, offering potential for practical applications in water treatment and energy generation.

To showcase the real-world potential of the catalyst, we have also tested the activity in actual textile wastewater collected from a local fabric dyeing centre. Remarkably, the CV–BV photocatalyst has not only achieved an impressive 96% degradation of pollutants under Xe lamp for 2 h but also simultaneously generated hydrogen at a substantial rate of 803.0 μmol $h^{-1}$ $g^{-1}$ (Fig. S11(a) and (b)). The photographs of textile wastewater before and after photocatalysis are shown in Fig. S11(c) and (d). This dual-action performance applied to real systems demonstrates the capability of the CV–BV system as a promising

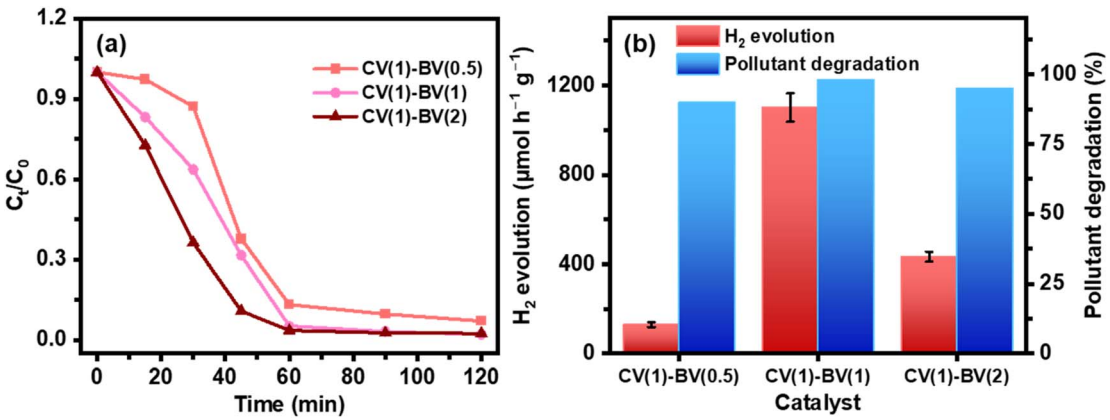


Fig. 7 (a) Time dependent degradation kinetics of MO in presence of CV–BV catalysts with different CV to BV molar ratio (b) simultaneous $H_2$ evolution and MO degradation rate of CV–BV catalyst with different ratios of BV.

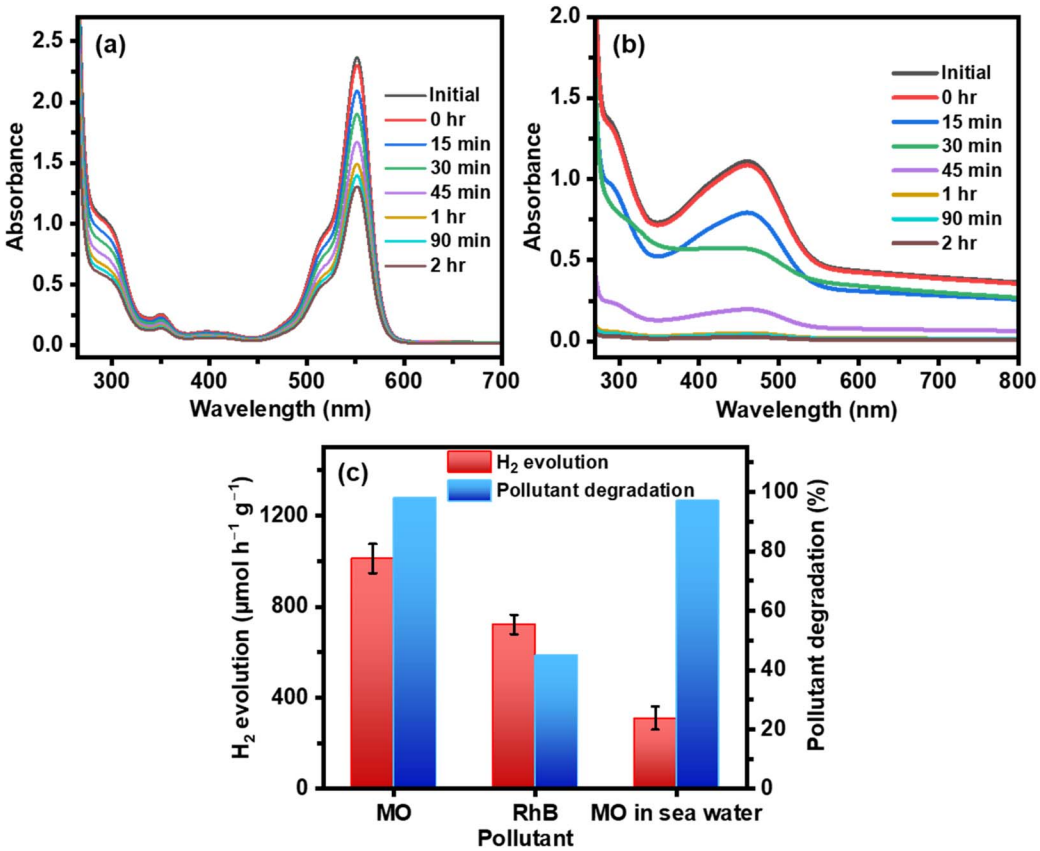


Fig. 8 UV-vis spectra showing photocatalytic degradation of (a) 20 ppm RhB dye in the presence of CV–BV in DI water and (b) MO dye in CV–BV catalyst in seawater (c) simultaneous $H_2$ evolution and pollutant (MO, RhB) degradation of CV–BV catalyst in DI water and simultaneous $H_2$ evolution rate and MO degradation of CV–BV catalyst in sea water.

candidate for sustainable environmental remediation and energy recovery.

### Radical trapping studies

To elucidate the mechanism underlying the photodegradation of organic pollutants, radical trapping experiments are conducted to identify the primary reactive species responsible for the degradation process. Specifically, the experiment has focused on determining the roles of superoxide radicals ($O_2^{\bullet-}$), hydroxyl radicals ($^{\bullet}OH$), and electrons ($e^-$) in the photodegradation of methyl orange (MO). Three specific scavengers are employed; benzoquinone (BQ) for trapping superoxide radicals, isopropyl alcohol (IPA) for hydroxyl radicals, and silver nitrate ($AgNO_3$) for electrons. Each scavenger is added to the reaction system at a concentration of 0.001 M, and the corresponding effects on degradation efficiency are carefully analysed and plotted in Fig. 9. The respective UV-vis absorption spectra of MO dye degradation in the presence of different radical trapping agents are provided in Fig. S12.

The degradation kinetics ($C_t/C_0$) given in Fig. 9(a) confirms the contribution of reactive species in the photodegradation mechanism of MO using the CV–BV emphasizing the dominant role of superoxide radicals and electrons. The addition of BQ significantly reduces the degradation efficiency from 98% to 45% in 2 h, as clearly illustrated in the bar diagram in Fig. 9(b), indicating that superoxide radicals play the most critical role in the photodegradation process. These results align with the impact of $AgNO_3$, which traps electrons that generate superoxide radicals. When $AgNO_3$ is introduced, the degradation efficiency drops to approximately 50%, demonstrating the interdependence of electrons and superoxide radicals in driving the photocatalytic reaction. In contrast, the introduction of IPA resulted in only a minor reduction in degradation efficiency, suggesting that hydroxyl radicals have a less significant role in this system.

### Stability and post-catalysis characterization

In order to assess the stability of the photocatalyst the CV–BV system is subjected to multiple cycles of simultaneous photocatalytic pollutant degradation and hydrogen evolution under identical reaction conditions. Between cycles, the photocatalyst is thoroughly cleaned using water and ethanol and dried at 60 °C. The CV–BV system demonstrated consistent rates of hydrogen evolution and pollutant degradation over five consecutive cycles, indicating excellent material stability Fig. 10(a) and (b) and the corresponding UV-vis absorbance plots are presented in Fig. S13.

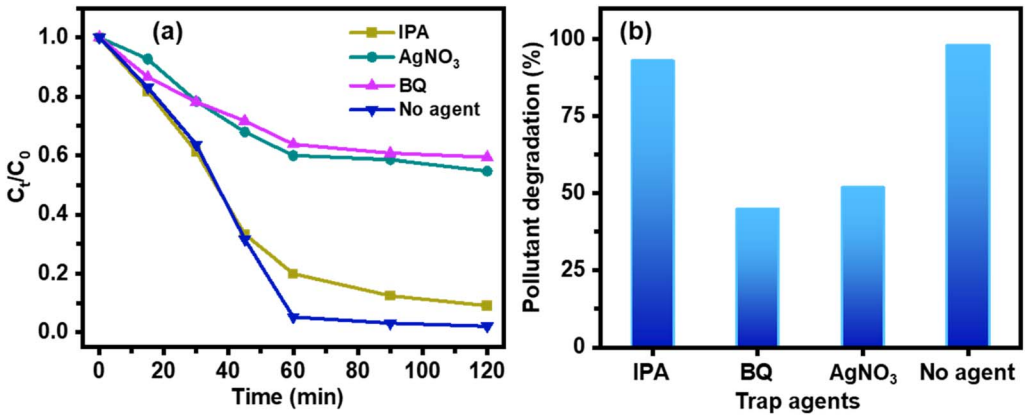


Fig. 9 (a) Kinetic plot and (b) bar diagram showing pollutant degradation percentage of radical trapping experiments for MO degradation performance of CV–BV in the presence of different scavengers.

The post-catalysis characterization is conducted using XRD, HRTEM and XPS as shown in Fig. 11 and 12. In Fig. 11(a), the diffraction peaks remain consistent with those of the fresh CV–BV sample as given earlier. Additionally, a few peaks appearing at 25.70°, 29.20°, 38.70°, and 52.30° post-catalysis can be assigned to the monoclinic crystal structure of $CeVO_4$, in agreement with the standard JCPDS data (CV 01-079-1066). The TEM images (Fig. 11(b) and (c)) of CV–BV after the photocatalytic reaction confirm that the material retains its original morphology without significant structural degradation. Lattice fringe analysis as shown in Fig. 11(c) further verifies the presence of characteristic planes of both CV and BV.

Additionally, the interface between CV and BV is distinctly visible in the figure, with the interface formation primarily facilitated by the planes of CV. This indicates the stability of the composite even after prolonged photocatalytic activity. Elemental mapping data (Fig. S14) confirms the uniform distribution of Ce, V, Bi, and O, demonstrating the structural integrity of the heterojunction. The EDS spectra (Fig. S15) and composition analysis (Table S2) further verify the presence of all expected elements, with no notable elemental loss or contamination, suggesting that CV–BV remains chemically stable after catalysis. These results highlight the stability of the material, making it a promising candidate for photocatalytic applications.

To further explore the structural integrity of the photocatalyst after the stability tests, additional characterization is performed using XPS analysis, as shown in Fig. 12. The Ce 3d spectra, as shown in Fig. 12(a), of CV–BV exhibit a 1 eV decrease in binding energy after the photocatalysis compared to that of as-synthesised CV–BV. This decrease in binding energy directly correlates with the reduction of $H^+$ facilitated by the catalyst. Notably, the ratio of $Ce^{3+}$ to $Ce^{4+}$ remains largely unchanged, indicating the retention of active defect sites and confirming the sustained activity of catalyst over extended use. The high-resolution Bi 4f spectra of post-catalytic CV–BV (Fig. 12(b)) reveal additional peaks at 161.10 eV and 166.70 eV, corresponding to $Bi^{5+}$ in Bi $4f_{7/2}$ and Bi $4f_{5/2}$, respectively, alongside the pre-existing $Bi^{3+}$. During the photocatalytic process, $Bi^{3+}$ in BV undergoes oxidation to $Bi^{5+}$, accompanied by the release of electrons. The V 2p spectra of the post-catalytic CV–BV samples (Fig. 12(c)) do not show any change in oxidation states compared to the as-synthesized CV–BV, although variations in XPS intensities are observed.

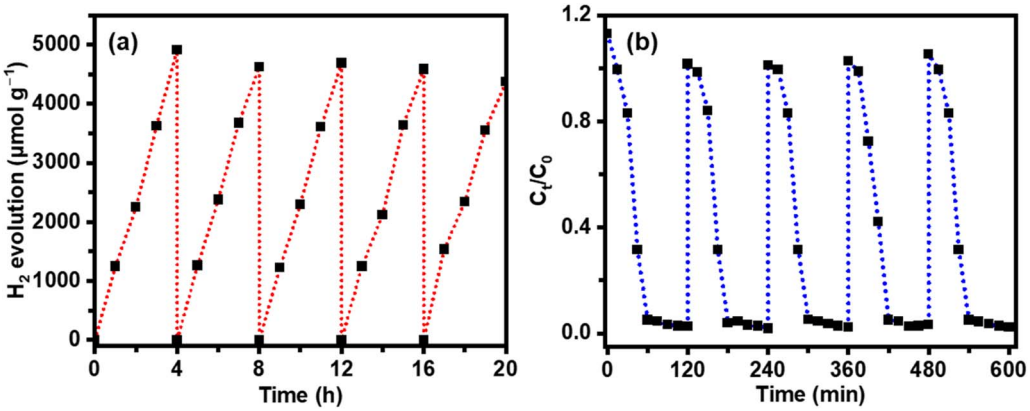


Fig. 10 Photocatalytic activity of CV–BV catalyst for multiple cycles towards simultaneous $H_2$ evolution and MO degradation (a) photocatalytic hydrogen production for 20 h, (b) photocatalytic degradation of MO for multiple usage of the catalyst.

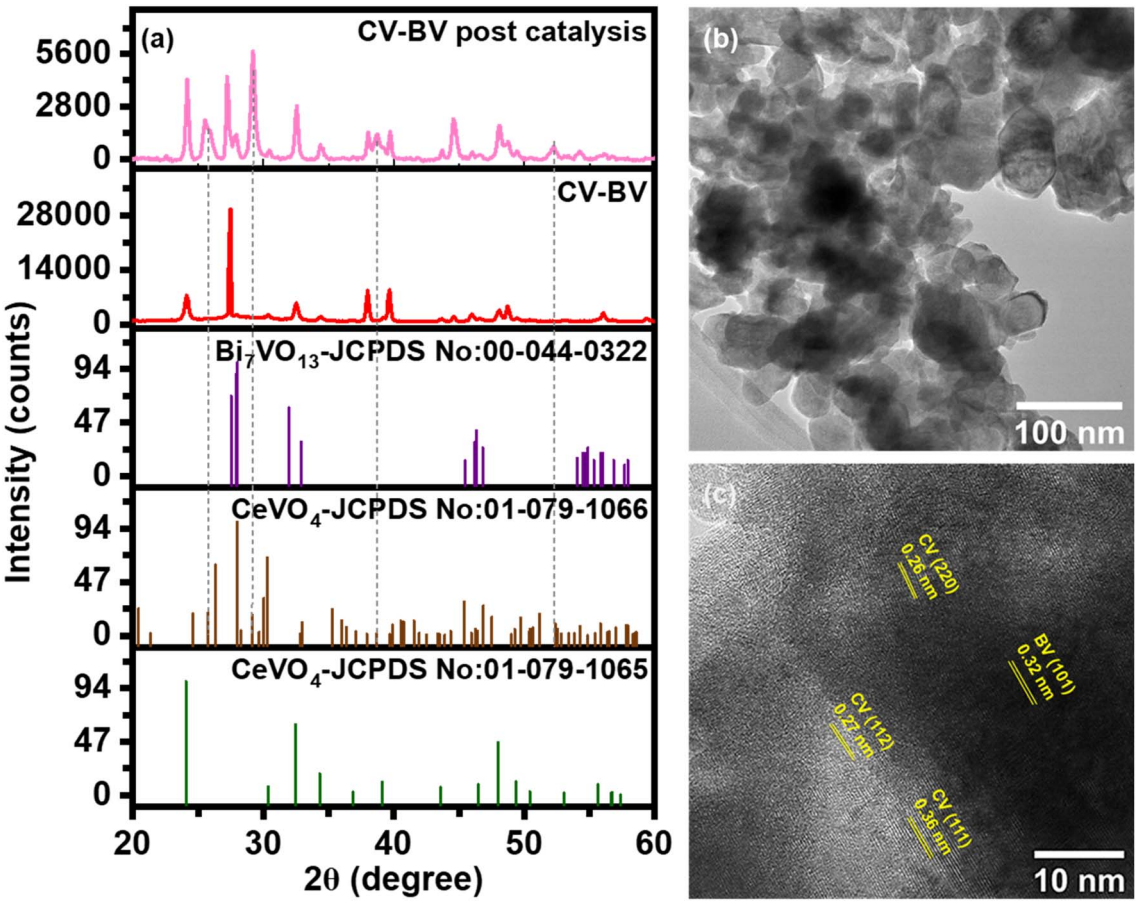


Fig. 11 XRD pattern of (a) CV–BV post-photocatalysis, as-synthesized CV–BV, standard JCPDS (b) HRTEM and (c) lattice planes resolved for CV–BV post-catalysis.

The post-catalytic O 1s spectra of CV–BV, show a significant variation in the amounts of $O_1$ and $O_2$. As illustrated in the Fig. 12(d), the intensity of $O_2$, corresponding to defect sites, has increased, while the intensity of $O_1$, representing lattice oxygen, has decreased in the post-catalytic CV–BV compared to the fresh CV–BV. This increase in defect sites is directly related to the enhanced charge separation facilitated by the CV–BV composite.

### Photocatalytic mechanism

From the combined results of UV-visible absorption spectra and valence band XPS analysis, the proposed photocatalytic mechanism of the CV–BV is illustrated in Fig. 13. This mechanism depicts the possible photoexcitation of electrons and holes, along with their electronic transfer over the photocatalyst surface under light illumination. The enhanced photocatalytic activity is attributed to the S-scheme charge transfer approach. The valence band potentials ($E_{VB,XPS}$) of CV and BV are determined to be 0.49 and 2.50 eV, respectively, based on their XPS valence band (VB-XPS) spectra (Fig. S16). The $E_{VB,NHE}$ values of CV and BV components are estimated to be 0.25 eV and 2.26 eV from the equation $E_{VB,NHE} = \Phi + E_{VB,XPS} - 4.44$, where $\Phi$ is the work function of the XPS instrument ($\Phi = 4.20$ eV) and $E_{VB,NHE}$ is the VB position *versus* NHE.[36] Moreover, according to the empirical formula, $E_{VB} = E_{CB} + E_g$, ($E_{CB}$ is the conduction band potential and $E_g$ is the bandgap obtained from Tauc plots), the $E_{CB}$ value of CV is estimated as −2.21 eV and that of the BV is 0.06 eV. These band levels facilitate the creation of the S-scheme heterojunction between CV and BV as illustrated in Fig. 13. When the CV–BV photocatalyst is exposed to light, it absorbs energy and gets photoexcited, leading to the generation of electron–hole pairs. At heterojunction interface, some of the photogenerated electrons in the conduction band of BV are transferred to the valence band of CV.[37] This directional transfer of electrons helps to suppress electron–hole recombination, thereby enabling efficient charge separation also supported by PL, photocurrent and impedance measurements, which is crucial for improving photocatalytic performance. Following this process, the electrons remaining in the conduction band of CV engage in redox reactions. These electrons react with water molecules or protons ($H^+$) in the system, facilitating the reduction process to produce molecular hydrogen. Concurrently, in the presence of MO solution, the photogenerated electrons in the conduction band of BV participate in the reduction of MO and initiates the breakdown of MO molecules. This S-scheme mechanism promotes the multifunctionality of the CV–BV photocatalyst. By enabling effective separation of

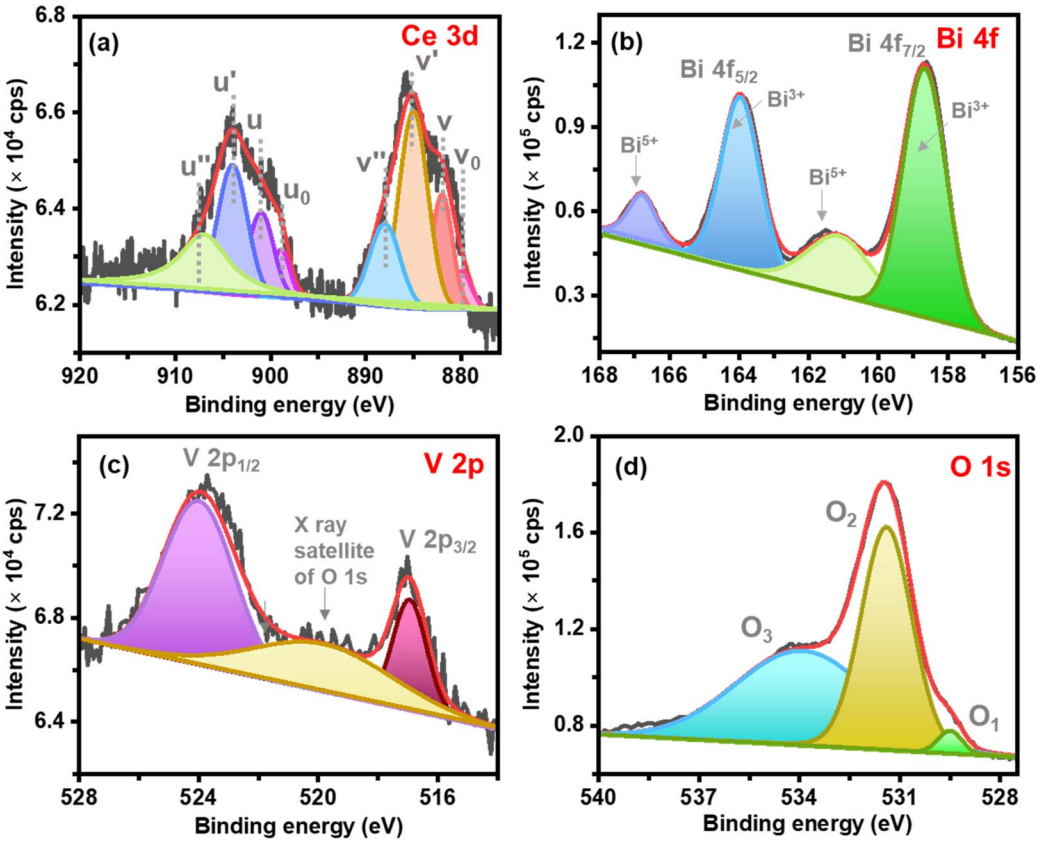


Fig. 12 (a) High resolution XPS scan of (a) Ce 3d, (b) Bi 4f (c) V 2p and (d) O 1s of CV–BV post-catalysis.

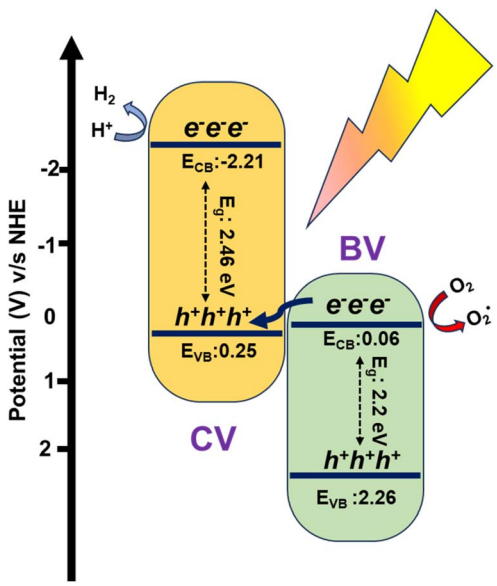


Fig. 13 The probable photocatalytic mechanism of CV–BV.

charge carriers, it supports simultaneous photocatalytic hydrogen evolution and organic pollutant degradation. Such a synergistic approach not only maximizes the utilization of photogenerated charge carriers but also demonstrates the potential of CV–BV as a robust system for addressing environmental pollution and contributing to sustainable energy generation.

## Conclusion

A cerium vanadate–bismuth vanadate composite material is successfully synthesized *via* a hydrothermal route and evaluated for its dual-purpose simultaneous photocatalytic activity. The engineered CV–BV heterostructure, operating through an S-scheme charge transfer pathway, has led to a substantial improvement in both hydrogen generation and pollutant breakdown compared to the individual constituents CV and BV. The optimized composite exhibits an impressive hydrogen evolution rate of 1011 μmol $h^{-1}$ $g^{-1}$ and a noteworthy 98% methyl orange removal efficiency, displaying its enhanced performance. A consistent catalytic activity is observed across five recycling runs, confirming its robust nature. Investigation of the reaction mechanism, utilizing scavenger studies, have revealed the primary involvement of superoxide radicals and electrons in the degradation process, along with secondary contributions from hydroxyl radicals. The S-scheme charge separation within the CV–BV system facilitates efficient light harvesting and charge migration, ultimately boosting its bifunctional catalytic capabilities. The CV–BV catalyst has showcased exceptional real-world performance when applied to untreated textile wastewater, achieving 96% degradation

efficiency alongside a high hydrogen evolution rate of 803.0 μmol $h^{-1}$ $g^{-1}$, emphasizing its robustness and practical utility in industrial settings. Furthermore, its efficiency is retained even in a saline environment, as demonstrated by 98% degradation and 310.0 μmol $h^{-1}$ $g^{-1}$ hydrogen generation in a methyl orange–seawater system. These results affirm the versatility and strong potential of the catalyst for integrated environmental remediation and green fuel recovery across diverse water streams. This work emphasizes the significant promise of the CV–BV composite as a viable option for simultaneous energy generation and pollutant degradation, paving the way for a more environmentally friendly future.

## Conflicts of interest

There are no conflicts of interest to declare.

## Data availability

Data will be made available on request.

Supplementary information is available: Tauc plots of CV and BV; TEM–EDS spectra, elemental mapping, EDS composition data of CV–BV; XPS survey spectra; GC calibration curve for hydrogen evolution; UV-vis absorbance spectra corresponding to photocatalytic degradation of 20 ppm dye with CV, BV, CV–BV composites, in sea water and actual wastewater, with different radical trapping agents, and multiple experimental cycles; LC-MS analysis and proposed degradation pathway; XRD patterns and UV-vis absorption spectra of CV–BV composites; hydrogen evolution data for various CV–BV dosages and actual wastewater; TEM-EDS and mapping data of post-catalytic CV–BV; valence band XPS spectra of CV and BV; GC traces for all hydrogen evolution experiments; a comparative table of simultaneous photocatalytic performance with recent literature reports. See DOI: **https://doi.org/10.1039/d5ra04077a**.

## Acknowledgements

The authors acknowledge CRF at CeNS for the characterization facility and JNCASR for the XPS facility. JRP and MV thank CeNS for fellowship.

## References

1 S. Kampouri and K. C. Stylianou, *ACS Catal.*, 2019, **9**, 4247–4270.
2 A. Al Miad, S. P. Saikat, M. K. Alam, M. S. Hossain, N. M. Bahadur and S. Ahmed, *Nanoscale Adv.*, 2024, **6**, 4781–4803.
3 X. Li, J. Wu, S. An, K. Li, J. Zhang, M. Pei, C. Song and X. Guo, *ACS Appl. Nano Mater.*, 2023, **6**, 11601–11611.
4 Y. Chai, Y. Chen, J. Shen, M. Ni, B. Wang, D. Li, Z. Zhang and X. Wang, *ACS Catal.*, 2021, **11**, 11029–11039.
5 W. Cheng, L. Wang, H. Lao, Y. Wei, J. Xu and B. Weng, *ACS Sustainable Chem. Eng.*, 2024, **12**, 17026–17034.
6 M. Lin, H. Chen, Z. Zhang and X. Wang, *Phys. Chem. Chem. Phys.*, 2023, **25**, 4388–4407.
7 A. Kumar, P. Sharma, G. Sharma, P. Dhiman, G. T. Mola, M. Farghali, A. K. Rashwan, M. Nasr, A. I. Osman and T. Wang, *Environ. Chem. Lett.*, 2024, **22**, 2405–2424.
8 Y. Yu, W. Li, Y. Huang, H. Yang, C. Lv, H. X. Yan, D. Lin, S. Jiao, L. Hou and Z. Wu, *Small*, 2024, **20**, 2309577.
9 L. Chen, D. Meng, X. Wu, A. Wang, J. Wang, Y. Wang and M. Yu, *J. Phys. Chem. C*, 2016, **120**, 18548–18559.
10 H. Q. Alijani, S. Iravani and R. S. Varma, *Catalysts*, 2023, **13**, 59.
11 Y. Pu, Y. Li, Y. Huang, S. I. Kim, P. Cai and H. J. Seo, *Mater. Lett.*, 2015, **141**, 73–75.
12 L. Li, Z. Zhang, D. Fang and D. Yang, *Inorg. Chem. Commun.*, 2024, **169**, 112971.
13 Y. H. Chiu, R. J. Chung, C. Kongvarhodom, M. Saukani, S. Yougbaré, H. M. Chen, Y. F. Wu and L. Y. Lin, *ACS Appl. Mater. Interfaces*, 2024, **16**, 11411–11422.
14 S. P. Kulkarni, Y. M. Chitare, V. V. Magdum, P. D. Sawant, S. V. Talekar, S. A. Pawar, D. B. Malavekar, S. Ansar, J. H. Kim and J. L. Gunjakar, *ACS Appl. Nano Mater.*, 2024, **7**, 11411–11422.
15 S. Mansour, R. Akkari, E. Soto, S. Ben Chaabene, N. Mota, R. M. Navarro Yerga, J. L. G. Fierro and M. S. Zina, *New J. Chem.*, 2021, **45**, 4481–4495.
16 K. Su, L. Zheng, M. Liu, J. Gao, Z. Shi, C. Chen, Y. Li, J. He and M. Peng, *Small*, 2024, **20**, 2405551.
17 F. A. Alharthi, A. El Marghany, N. A. Y. Abduh and I. Hasan, *Phys. Status Solidi A*, 2024, **221**, 2300743.
18 M. Amarnath and K. Gurunathan, *Sens. Actuators, B*, 2021, **336**, 129679.
19 Y. Li, K. Li, Y. Liu and Y. Gong, *Nanoscale*, 2022, **14**, 16673–16682.
20 L. Ding, Q. Han, H. Lu, Y. Yang, G. Lu, H. Zhang, X. Ran, Y. Xia, P. Li, Y. Chen and Y. Zhou, *Catalysts*, 2021, **11**, 1115.
21 X. Han, B. Li, W. Wang, B. Feng, Q. Tang, Y. Qi, R. Zhao, W. Qiu, S. Zhao, Z. Pan, X. Guo, H. Du, J. Qiu, H. Liu, G. Li and H. Xue, *ACS Nano*, 2024, **18**, 19836–19853.
22 G. Lu, Z. Lun, H. Liang, H. Wang, Z. Li and W. Ma, *J. Alloys Compd.*, 2019, **772**, 122–131.
23 X. Cui, Z. Liu, G. Li, M. Zhang, Y. Song and J. Wang, *Int. J. Hydrogen Energy*, 2019, **44**, 23921–23935.
24 H. Liu, Y. Zhang, D. Li, Y. Li and Z. Jin, *ACS Appl. Energy Mater.*, 2022, **5**, 2474–2483.
25 H. Noh, J. Lee, H. Ma, J. Shin, I. Roh, J. Yang and T. Yu, *J. Ind. Eng. Chem.*, 2023, **125**, 277–283.
26 R. Suo, L. Xie, Z. Hu, S. Wang, J. Chen and C.-Z. Lu, *J. Rare Earths*, 2024, DOI: **10.1016/j.jre.2024.08.014**.
27 A. Zonarsaghar, M. Mousavi-Kamazani and S. Zinatloo-Ajabshir, *Ceram. Int.*, 2021, **47**, 35248–35259.
28 B. Sriram, S. Kogularasu, S. F. Wang and G. P. Chang-Chien, *ACS Appl. Nano Mater.*, 2024, **7**, 17295–17304.
29 M. Hu, W. Ji, L. Wang, S. Lv, Q. Zhao and Y. Hao, *J. Mater. Sci.: Mater. Electron.*, 2022, **33**, 26157–26166.
30 H. T. T. Nguyen, D. Jung, C. Y. Park and D. J. Kang, *Mater. Chem. Phys.*, 2015, **165**, 19–24.
31 Q. Qin, Q. Cai, C. Jian and W. Liu, *Sustainable Energy Fuels*, 2021, **5**, 1129–1133.

32 S. Jayachitra, D. Mahendiran, P. Ravi, P. Murugan and M. Sathish, *Appl. Catal., B*, 2022, **307**, 121159.
33 R. Wakimoto, T. Kitamura, F. Ito, H. Usami and H. Moriwaki, *Appl. Catal., B*, 2015, **166**, 544–550.
34 Y. Yang, Z. Wu, R. Yang, Y. Li, X. Liu, L. Zhang and B. Yu, *Appl. Surf. Sci.*, 2021, **539**, 148220.
35 A. Ajmal, I. Majeed, R. N. Malik, H. Idriss and M. A. Nadeem, *RSC Adv.*, 2014, **4**, 37003–37026.
36 C. T. Blaise, M. W. Chu, P. Y. Chen, J. W. Chen, C. S. Tu and W. S. Chang, *Ceram. Int.*, 2023, **49**, 6324–6331.
37 X. H. Jiang, L. C. Wang, F. Yu, Y. C. Nie, Q. J. Xing, X. Liu, Y. Pei, J. P. Zou and W. L. Dai, *ACS Sustainable Chem. Eng.*, 2018, **6**, 12695–12705.